Cryogenics 90 (2018) 30–40

Contents lists available at ScienceDirect

Cryogenics

journal homepage: www.elsevier.com/locate/cryogenics

Research paper

# CFD modeling and experimental verification of oscillating flow and heat transfer processes in the micro coaxial Stirling-type pulse tube cryocooler operating at 90–170 Hz

Yibo Zhao[a], Guorui Yu[a], Jun Tan[b], Xiaochen Mao[a], Jiaqi Li[b,c], Rui Zha[b,c], Ning Li[b], Haizheng Dang[b,*]

[a] Shanghai Institute of Measurement and Testing Technology, 1500 Zhangheng Road, Shanghai 201203, China
[b] State Key Laboratory of Infrared Physics, Shanghai Institute of Technical Physics, Chinese Academy of Sciences, 500 Yutian Road, Shanghai 200083, China
[c] University of Chinese Academy of Sciences, No. 19A Yuquan Road, Beijing 100049, China

ARTICLE INFO

*Keywords:*
CFD modeling
Oscillating flow and heat transfer
90–170 Hz
Micro coaxial Stirling-type pulse tube cryocooler
Experimental verification

ABSTRACT

This paper presents the CFD modeling and experimental verifications of oscillating flow and heat transfer processes in the micro coaxial Stirling-type pulse tube cryocooler (MCSPTC) operating at 90–170 Hz. It uses neither double-inlet nor multi-bypass while the inertance tube with a gas reservoir becomes the only phase-shifter. The effects of the frequency on flow and heat transfer processes in the pulse tube are investigated, which indicates that a low enough frequency would lead to a strong mixing between warm and cold fluids, thereby significantly deteriorating the cooling performance, whereas a high enough frequency would produce the downward sloping streams flowing from the warm end to the axis and almost puncturing the gas displacer from the warm end, thereby creating larger temperature gradients in radial directions and thus undermining the cooling performance. The influence of the pulse tube length on the temperature and velocity when the frequencies are much higher than the optimal one are also discussed. A MCSPTC with an overall mass of 1.1 kg is worked out and tested. With an input electric power of 59 W and operating at 144 Hz, it achieves a no-load temperature of 61.4 K and a cooling capacity of 1.0 W at 77 K. The changing tendencies of tested results are in good agreement with the simulations. The above studies will help to thoroughly understand the underlying mechanism of the inertance MCSPTC operating at very high frequencies.

## 1. Introduction

In recent years, the miniaturization of the low-temperature sensors has attracted worldwide attention. Many of these applications are based on optical and electronic technologies and only require relatively small cooling powers, typically 1 W-class or less, but they do need very short cooldown time, which have a strong appeal to the defense field since the military operations usually need to cool quickly to the operating temperature in order to enable rapid deployment. However, up until now, there still exists a wide gap between the rapid development of the low-temperature sensors and the availability of the applicable miniaturized cryocoolers [1]. In some senses, the miniaturized low-temperature applications would be more widespread now if it were not for the problems associated with the cryocoolers needed to cool them. For example, a certain recuperative cryocooler named the open-loop Joule-Thomson cryocooler (JT) has acted as the traditional backbone of the rapid cooldown cryocoolers for a long time. Easily miniaturized resulting from the absence of any moving component at the cold end, together with a very high charge pressure (such as larger than 20 MPa), the open-loop JT can achieve a very rapid cooldown, typically a few seconds to 77 K, thereby becoming an ideal candidate for cooling infrared sensors used in the missile guidance. However, a series of serious disadvantages such as the susceptibility to plugging of the valve, the intrinsic inefficiency and especially, the very short cooling duration (cooling lasts for only a few minutes) make it impossible to be used in numerous important applications requiring reliable, efficient cooling and a much longer cooling duration. More recently, there is a growing interest in miniaturizing regenerative cryocoolers such as the Stirling cryocooler and the Stirling-type pulse tube cryocooler (SPTC). The charge pressure in them is much lower, typically only 1–5 MPa, but the cooling efficiency is generally several times that of the open-loop JT. Especially for the SPTC, similar to the JT, there is also no moving component at the cold end, thereby greatly facilitating the miniaturization. Compared with the Stirling cryocooler, the SPTC is also well

* Corresponding author.
*E-mail address:* haizheng.dang@mail.sitp.ac.cn (H. Dang).

https://doi.org/10.1016/j.cryogenics.2018.01.003
Received 6 September 2017; Received in revised form 29 November 2017; Accepted 5 January 2018
Available online 05 January 2018
0011-2275/ 

**Nomenclature**

| | |
|---|---|
| $f$ | operating frequency (Hz) |
| $I$ | input current (A) |
| $L_{pt}$ | pulse tube length (m) |
| $\dot{m}$ | mass flow rate (kg/s) |
| $p$ | pressure (Pa) |
| $p_0$ | charging pressure (Pa) |
| $\Delta p$ | amplitude of the dynamic pressure (Pa) |
| $R$ | coil resistance (Ω) |
| $t$ | time (s) |
| $T$ | temperature (K) |
| $v$ | velocity (m/s) |
| $\langle \dot{W}_{pv} \rangle$ | input PV power (W) |
| $\dot{W}_e$ | input electric power (W) |

*Greek symbols*

| | |
|---|---|
| $\alpha$ | permeability ($m^2$) |
| $\varepsilon$ | porosity |
| $\mu$ | viscosity (Pa s) |
| $\rho$ | density ($kg/m^3$) |
| $\bar{\bar{\tau}}$ | stress tensor ($N/m^2$) |
| $\eta$ | motor efficiency |
| $\varphi$ | phase angle (rad) |
| $\tau$ | period (s) |
| $\theta_m$ | phase angle between dynamic pressure and mass flow rate (rad) |
| $\theta_v$ | phase angle between dynamic pressure and velocity (rad) |

*Subscripts*

| | |
|---|---|
| ai | aftercooler inlet |
| f | fluid |
| s | solid matrix |
| h | warm end |
| c | cold end |
| in | pulse tube inlet |
| out | pulse tube outlet |
| mid | pulse tube midpoint |
| opt | optimal value |

known for its long life and high reliability, for example, some excellent SPTCs could continuously operate in orbit for over 10 years and has already widely been acknowledged as a new-generation space cryocooler [2–6]. Therefore, recently there is a continuously increasing interest in the miniaturization of the SPTC, potentially used either in space or on ground.

Normally, the cooling capacity of a regenerative cryocooler would decrease sharply with the reduction in size, and an effective solution to this problem is to increase both the charge pressure and the cycle frequency to compensate for the decrease in working fluid volume [1]. However, a too high operating frequency often results in the poor heat transfer in the regenerative heat exchanger, thereby producing considerable irreversible losses. A frequency of about 60 Hz has been ever considered to be the maximum frequency that could be used while maintaining high efficiency for a SPTC [1].

A few of theoretical analyses were made about reducing the size while maintaining the cooling efficiency of a regenerative cryocooler. For example, Peterson and Al Hazmy [7] and Shire et al. [8] tried to establish a theoretical lower size limit to the miniaturization. Radebaugh and O'Gallagher [9] tried to find out the operating parameters and regenerator geometries necessary to design viable high frequency miniature cryocoolers, and concluded through modeling that it was possible to maintain high efficiency even for frequencies of several hundred hertz. Several impressive progresses were also made in experimentally miniaturizing SPTCs. For example, Petach et al. [10] developed a 782 g MCSPTC prototype operating at about 100 Hz with a cooling capacity of 1.1 W at 77 K for space applications, which later evolved into an Engineering Model (EM) [11,12] weighing 857 g capable of lifting 1.3 W at 77 K with an expected lifetime of over 10 years, and recently both of its working temperature range and cooling capacities were further extended to 5 W at 150 K or more than 0.3 W at 45 K [13]. Olson et al. [14] designed a 310 g MCSPTC prototype operating at 100 Hz around capable of 650 mW at 150 K for both tactical and space applications, whose 328 g space version EM with a predicted 10-year-lifetime underwent qualification to a technology readiness level (TRL) of 6 [15], and recently the TRL 6 version was further modified to a weight of about 450 g and thus significantly increased the cooling capability to 2 W at 105 K [16]. Several other attempts were also made on the in-line or coaxial SPTCs, however, either the miniaturization of the linear compressors was not realized or the mismatch between compressor and cold finger occurred [17,18]. Especially, up till now, the relevant studies mainly focus on the structural design and manufacture while systematic studies about the physical mechanism and flow characteristics inside the MCSPTC were seldom made.

The CFD method is an effective approach of systematically analyzing the internal process in a SPTC. For the mid- or large-sized SPTCs operating at frequencies below 60 Hz, several two-dimensional CFD models were ever suggested to simulate the flow and heat transfer processes in the system [19–21]. About the micro SPTC operating at considerably high frequencies, two authors of this paper [22] recently established a two-dimensional axis-symmetric CFD model of a MCSPTC weighting 920 g operating at 128 Hz, and analyzed the regenerator losses and the cooler performance characteristics at the fixed frequency by considering both thermal equilibrium and non-equilibrium models of the porous matrix. However, the above analyses did not discuss a wider operating frequency range. This paper will significantly extend the range to 90–170 Hz, and moreover, the pulse tube length will not be fixed anymore.

The function of the pulse tube is to insulate the processes at its two ends, in which the working fluid oscillates back and forth. But in some cases, the streaming or DC flow will occur within the pulse tube and thus carry a large enthalpy flow from warm to cold end, thereby

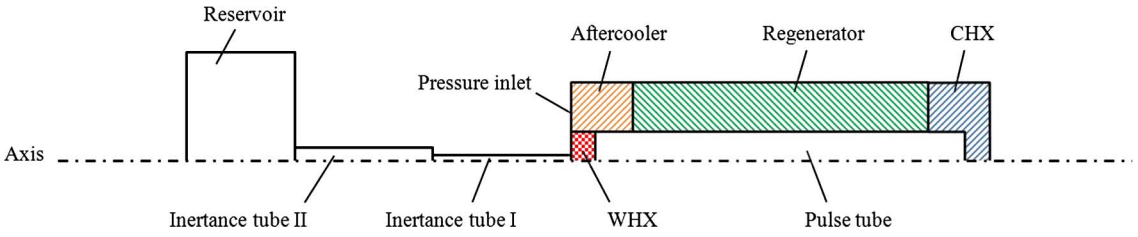


**Fig. 1.** 2-D axisymmetric CFD model of the MCSPTC.

deteriorating the cooling performance. A few of typical DC flows such as Gedeon flow [23] and Rayleigh flow [24] were ever observed and the corresponding suppression methods were proposed, but the investigations were mainly focused on the SPTC with the middle size typically operating at lower frequencies of 30–60 Hz. In this paper, the effects of the much higher operating frequencies of 90–170 Hz on the cooler performance and flow characteristics will be analyzed in detail, and the influence of the pulse tube length on the temperature and velocity oscillations in the given frequency range will also be discussed. In order to verify the theoretical results and analyses, the MCSPTC operating at 90–170 Hz without either double-inlet or multi-bypass will be designed and manufactured, and the experimental verifications will be carried out.

## 2. Simulation results and discussions

Fig. 1 gives the CFD model of the MCSPTC [22]. The geometrical dimensions and boundary conditions for each component are listed in Table 1, in which the length of the pulse tube is a variable. The linear compressor is modeled as an oscillating pressure inlet in all cases, which is given by:

$$p_{ai} = p_0 + \Delta p \sin 2\pi f t \quad (1)$$

where $f$ is the operating frequency, $p_0$ is the charging pressure, and $\Delta p$ is the amplitude of the dynamic pressure at the pressure inlet. The values of $p_0$ and $\Delta p$ are fixed at 3.6 MPa and 0.377 MPa, respectively.

### 2.1. Basic case

As shown in Table 2, Case 1 operating at 128 Hz with a 30 mm-long pulse tube is considered to be the basic case, which could achieve a no-load temperature of 64.5 K [17] in the model. Here the oscillating flow and heat transfer processes in the pulse tube in Case 1 will be investigated first, and the flow characteristics at three special cross-sections such as the inlet, midpoint and outlet of the pulse tube will be focused on.

Fig. 2 shows the temporal variations of the cross-sectional averaged axial velocity at the inlet, midpoint and outlet of the pulse tube in Case 1. $\varphi = 0$ and $\varphi = \pi$ represent the states when the inlet pressure reaches the maximum and minimum, respectively. The velocity of the fluid flowing from cold to warm end is positive. It can be observed that all of the three curves are very close to the sinusoidal waves, and the amplitude of the axial velocity at the inlet is 3.52 m/s, about 1.27 m/s and 2.32 m/s lower than those at the midpoint and the outlet, respectively, which indicates that the velocity increases from cold to warm end. In addition, the phase of the velocity at the outlet lags those at the midpoint and the inlet about 0.053π and 0.079π, respectively, which means that the impedance near the warm end is a little higher than that near the cold end.

Fig. 3 shows the temporal variations of the mass flow rate at the inlet, midpoint and outlet of the pulse tube in Case 1. The positive value also represents the fluid flowing from cold to warm end. The curves at both inlet and outlet are still appropriate to sine waves. However, the temporal variation of the mass flow rate at the midpoint is far away from the sinusoidal oscillation, in which the increasing duration accounts for 66% in a cycle, nearly doubling the decreasing time. This phenomenon indicates that the flow condition is complicated in the middle segment of the pulse tube, and the streaming might occur within it.

Fig. 4 shows the temporal variations of the cross-sectional averaged temperature at the inlet, midpoint and outlet of the pulse tube in Case 1. It is observed that the changing tendencies of the three curves are completely different from each other, in which only the temperature cycling at the midpoint shows an approximately sinusoidal oscillation with an amplitude of about 92 K. However, the temperature differences between the maximum and minimum are only 6.7 K and 32.5 K at cold and warm ends, respectively, which indicates that the temperature fluctuation in the middle segment is much larger than those near both two ends in Case 1. Furthermore, the curve at the outlet is more complicated than the other two, in which the temperature increases sharply from the lowest point, then experiences a stable period of about 0.85π before reaching the peak, and finally decreases gradually from the maximum. Our analyses show that the complicated changing tendencies at both warm and cold ends are mainly caused by the heat transfer between the pulse tube and the corresponding heat exchangers.

Fig. 5(a) and (b) show the temperature contours inside the pulse tube at different states over a cycle in Case 1. It indicates that the gas in the pulse tube can be divided by three segments, in which the middle segment actually acts as the gas displacer, which only oscillates inside the pulse tube but never moves out of it, thereby isolating the gases at both ends. From $\varphi = 0$ to $\varphi = \pi$, the gas inside the pulse tube experiences the expansion process, in which the gas temperature goes down and the CHX absorbs the heat. By contrast, the gas experiences the compression process from $\varphi = \pi$ to $\varphi = 2\pi$ (0) and the WHX gives up the heat. These processes are also indicated in Fig. 6, which shows the temperature profiles of the pulse tube wall at different states over a cycle. The temperature distributions when $\varphi$ is equal to 0 or $3\pi/2$ are much higher than the other two states. Fig. 5(a) and (b) also show that the isotherms in the pulse tube are distorted, especially during the compression process, which leads to a mix, to some extent, between adjacent warmer and colder fluids, and thus may worsen the cooling performance.

### 2.2. Effect of operating frequency

The basic operating frequency of 128 Hz is the optimum value gotten from the 1-D numerical simulation. However, for the 2-D CFD model considering the multi-dimensional flow effects, the optimal operating frequency should be found again. A series of operating frequencies ranging from 90 to 170 Hz are thus employed in Cases 2–9.

The input PV power can be calculated by:

$$\langle \dot{W}_{pv} \rangle = \frac{1}{\rho_f \tau} \int_0^\tau p_{ai} \dot{m}_{ai} \cos\theta_m dt \quad (2)$$

where $\rho_f$ is the fluid density, $\tau$ is the period. $p_{ai}$ and $\dot{m}_{ai}$ represent the pressure and the mass flow rate at the inlet of the aftercooler, respectively, and $\theta_m$ is the phase difference between them.

Table 3 gives the input PV powers in Cases 2–9, where $|\dot{m}_{ai}|$ is the amplitude of the mass flow rate at the aftercooler inlet. It shows that the input PV power only changes slightly in the cases, which indicates that when the cooling performance, oscillating flow and heat transfer processes at different frequencies are studied, the amplitude of the input dynamic pressure keeps constant and the input PV power varies slightly. And thus the comparisons for the cases are reasonable.

Fig. 7 shows the time-averaged no-load temperatures as a function of the operating frequency in Cases 1–9. The best performance occurs in Case 6 for 140 Hz, which achieves a no-load temperature of 51 K, about 13.5 K lower than 64.5 K in Case 1. The worst one occurs at 90 Hz, which only reaches about 158 K. The results show that 128 Hz is no

**Table 1**
Geometrical dimensions and boundary conditions.

| Component | Radius (mm) | Length (mm) | Boundary condition |
|---|---|---|---|
| Aftercooler | 6.5 | 5 | Tw = 300 K |
| Regenerator | 6.5 | 24 | Adiabatic |
| CHX | 6.5 | 5 | Adiabatic |
| Pulse tube | 2.5 | Variable | Adiabatic |
| WHX | 2.5 | 2 | Tw = 300 K |
| Inertance tube 1 | 0.85 | 560 | Tw = 300 K |
| Inertance tube 2 | 1.05 | 720 | Tw = 300 K |
| Reservoir | 15 | 40 | Tw = 300 K |

**Table 2**
Variables in each case.

| Case number | Operating frequency (Hz) | Pulse tube length (mm) |
|---|---|---|
| 1 | 128 | 30 |
| 2 | 90 | 30 |
| 3 | 100 | 30 |
| 4 | 110 | 30 |
| 5 | 120 | 30 |
| 6 | 140 | 30 |
| 7 | 150 | 30 |
| 8 | 160 | 30 |
| 9 | 170 | 30 |
| 10 | 170 | 27.5 |
| 11 | 170 | 25 |
| 12 | 170 | 22.5 |
| 13 | 170 | 20 |

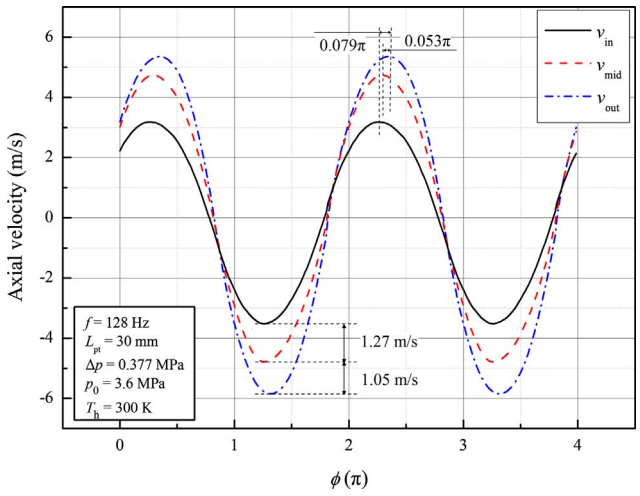


**Fig. 2.** Variations of the cross-sectional averaged axial velocity at the inlet, midpoint and outlet of the pulse tube in Case 1.

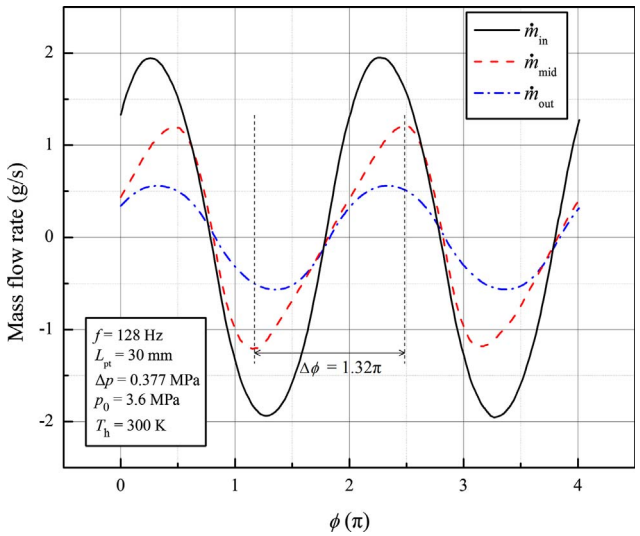


**Fig. 3.** Variations of the mass flow rate at the inlet, midpoint and outlet of the pulse tube in Case 1.

longer the optimum frequency for this 2-D CFD model, and the performance of the MCSPTC is heavily dependent on the operating frequency.

Fig. 8 shows the amplitudes of the cross-sectional averaged axial velocity at the inlet, midpoint and outlet of the pulse tube ranging from 90 to 170 Hz. All of the three curves share the similar changing

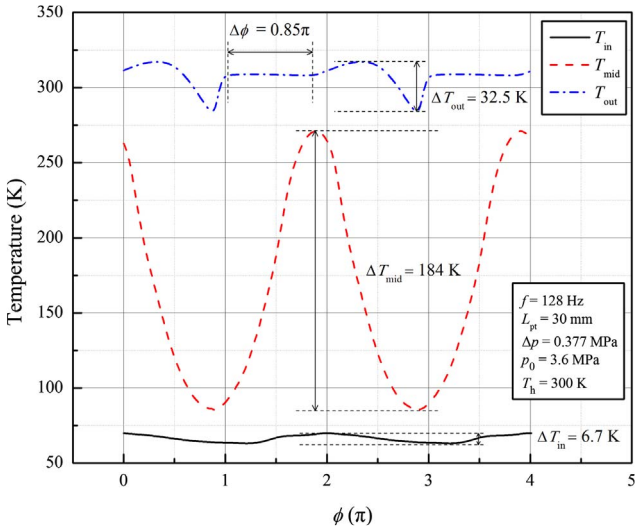


**Fig. 4.** Variations of the cross-sectional averaged temperature at the inlet, midpoint and outlet of the pulse tube in Case 1.

tendency in which the velocity amplitude decreases linearly with the increasing operating frequency, and the decreasing slopes for the three cross-sections are approximately the same with each other. The general rule that the velocity increases from cold to warm end in the basic case is also applicable to Cases 2–9. Furthermore, Fig. 8 also shows the variations of the phase angle between the dynamic pressure and velocity at the inlet and outlet of the pulse tube as a function of the operating frequency. The positive value means the phase of the mass flow lags behind the pressure wave. It can be observed that, the phase angle at the inlet fluctuates between 0.20$\pi$ and 0.26$\pi$, and that at the outlet varies between 0.25$\pi$ and 0.32$\pi$, both of which have little changes with the variation of the operating frequency provided that the geometric dimensions of components keep constant.

However, a distinctly different phenomenon is observed about the amplitudes of the mass flow rate at the inlet, midpoint and outlet of the pulse tube as a function of the operating frequency, as shown in Fig. 9. Except that the amplitude of the mass flow rate at the outlet still decreases linearly from 90 to 170 Hz, the value at the inlet increases gradually from 90 Hz until reaching its maximum at 140 Hz, and then drops sharply from 140 to 170 Hz. Moreover, an abrupt turn occurs at between 140 Hz and 150 Hz in the curve at the midpoint. Therefore, it can be concluded that the optimum frequency of 140 Hz is a turning point, and the mass transfer processes are markedly different before and after the point. The more detailed analyses will be discussed as follows with the aid of the temperature contours and the velocity streamlines. Fig. 9 shows the phase differences between the dynamic pressure and the mass flow at the inlet and outlet of the pulse tube as a function of the operating frequency. The positive value represents the pressure wave leads the mass flow rate. Likewise in Fig. 8, the two curves also indicate that the operating frequency has little effects on the phase relationship between the mass flow and the pressure wave if the cooler size keeps constant.

Fig. 10 shows the temporal variations of the cross-sectional averaged temperature at the outlet of the pulse tube in Cases 2, 4, 6 and 9, respectively. It can be observed that, the changing tendencies in all of the four cases are similar to that in the basic case shown in Fig. 4, but the oscillating range is quite different from each other, in which the highest temperature is nearly the same whereas the lowest temperature is heavily affected by the operating frequency. The smallest temperature difference of 23.2 K is achieved in Case 6 at 140 Hz, about 44.8 K and 74.3 K smaller than those in Case 4 at 110 Hz and in Case 2 at 90 Hz, respectively, which indicates that a strong mixing between warm and cold fluids occurs near the warm end when the operating frequency

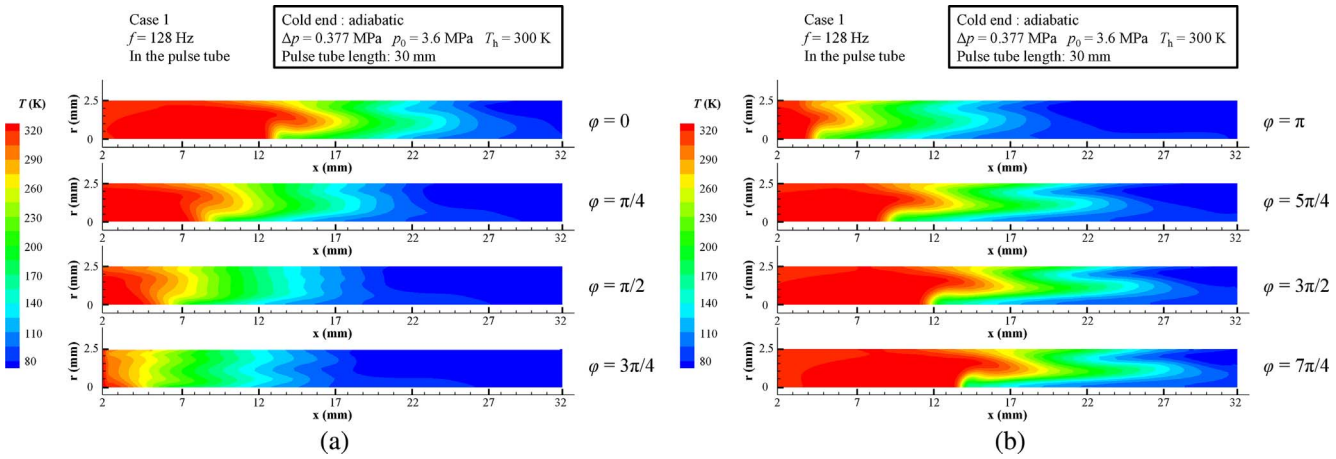


**Fig. 5.** Temperature contours inside the pulse tube during one cycle in Case 1. (a) $\varphi = 0$ to $\varphi = 3\pi/4$. (b) $\varphi = \pi$ to $\varphi = 7\pi/4$.

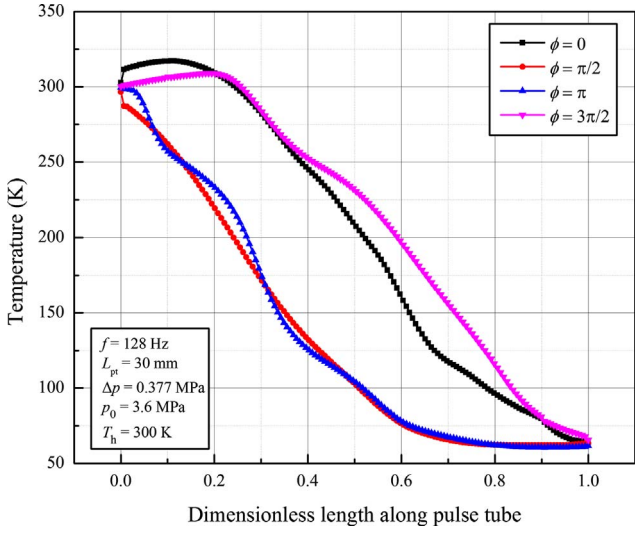


**Fig. 6.** Temperature profiles of the pulse tube wall during one cycle in Case 1.

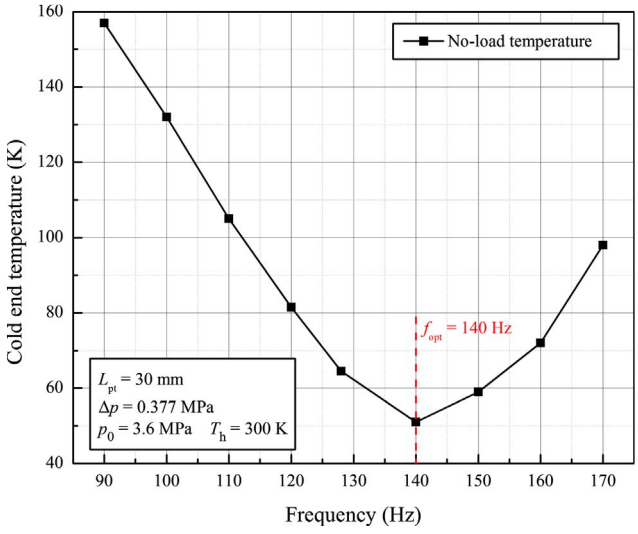


**Fig. 7.** Time-averaged no-load temperature as a function of the operating frequency.

**Table 3**
Input PV power in cases 2–9.

| Case number | Operating frequency (Hz) | $\lvert\dot{m}_{ai}\rvert$ (g/s) | $\langle\dot{W}_{pv}\rangle$ (W) |
|---|---|---|---|
| 2 | 90 | 1.21 | 39.4 |
| 3 | 100 | 1.23 | 40.3 |
| 4 | 110 | 1.26 | 41.1 |
| 5 | 120 | 1.28 | 42.0 |
| 6 | 140 | 1.31 | 42.7 |
| 7 | 150 | 1.33 | 43.2 |
| 8 | 160 | 1.34 | 43.3 |
| 9 | 170 | 1.35 | 43.5 |

is much lower than the optimum. However, the temperature difference in Case 9 at 170 Hz is only 27.4 K, a little larger than that at 140 Hz, which means that the mix near the warm end is not strong with the frequency much higher than the optimum.

Fig. 11 shows the temporal variations of the cross-sectional averaged temperature at the midpoint of the pulse tube in Cases 2, 4, 6 and 9, respectively. The wave shapes for the four cases are quite different. An approximately trapezoidal wave can be observed in Case 2 at 90 Hz, in which both the increasing and decreasing durations are much shorter than the stable period. The shape in Case 4 at 110 Hz is between sinusoidal and trapezoidal, and that in Case 6 at 140 Hz shows an approximately sinusoidal variation. The above results indicate that the temperature oscillating at the midpoint of the pulse tube is far away

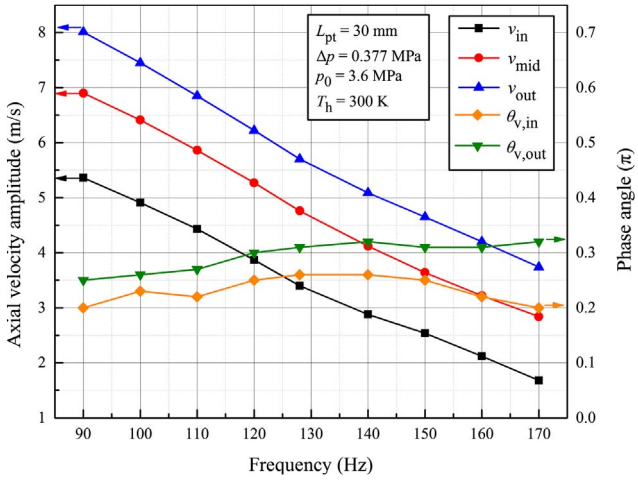


**Fig. 8.** Amplitudes of the cross-sectional averaged axial velocity with the phase angle at the inlet, midpoint and outlet of the pulse tube as a function of the operating frequency.

from the sine wave with a much lower operating frequency than the optimum, thereby deteriorating the cooling performance. The variation in Case 9 at 170 Hz is also similar to a sinusoidal wave, however, its amplitude is much smaller than that in Case 6 at 140 Hz, which is in accordance with the comparisons of the mass flow rates at the midpoint

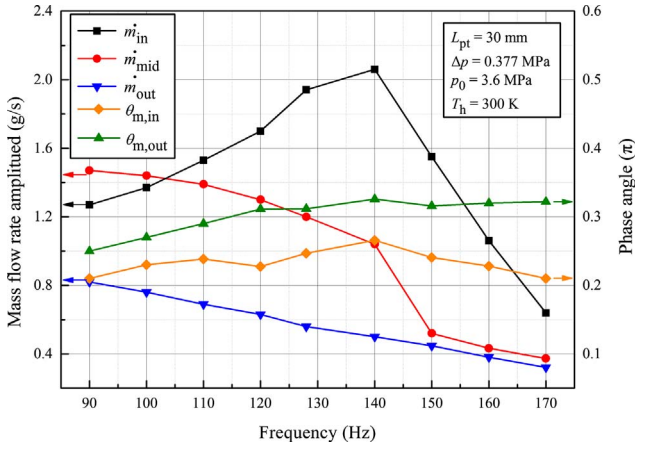


**Fig. 9.** Amplitudes of the mass flow rate with the phase angle at the inlet, midpoint and outlet of the pulse tube as a function of the operating frequency.

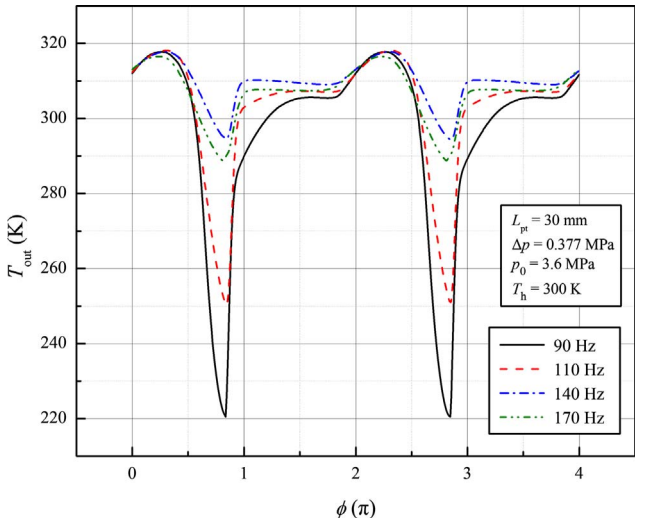


**Fig. 10.** Variations of the cross-sectional averaged temperature at the outlet of the pulse tube in Cases 2, 4, 6 and 9.

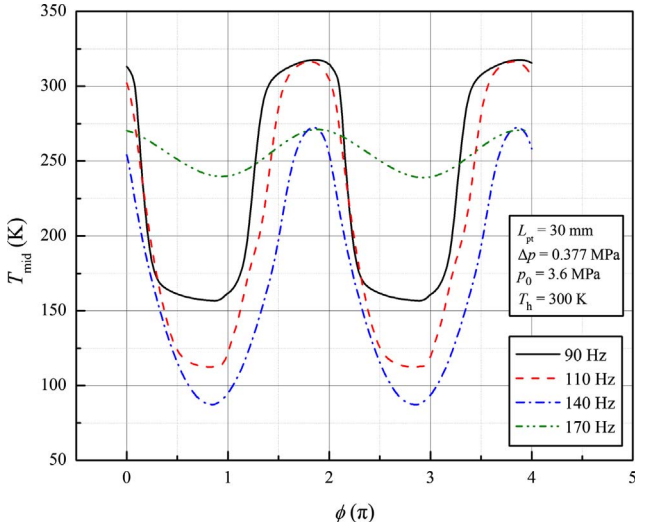


**Fig. 11.** Variations of the cross-sectional averaged temperature at the midpoint of the pulse tube in Cases 2, 4, 6 and 9.

shown in Fig. 9. It can be predicted that the flow intensity in the middle segment of the pulse tube becomes quite weaker with the frequency much higher than the optimum.

Figs. 10 and 11 only show the variations of the cross-sectional averaged temperature at two special cross-sections. The multi-dimensional flow effects on the temperature variations in the whole pulse tube can be observed more clearly by temperature contours. Fig. 12(a–f) show temperature contours inside the pulse tube in four different situations during one cycle in Cases 2, 4 and 6–9, respectively. The variations of temperature contours over one cycle can be used to explain the effect of the operating frequency on the cooling performance. Either upper or lower temperature limit for each case is different so that the temperature variations from warm to cold end can be displayed more clearly. It is observed that the gas inside the pulse tube operating at different frequencies experiences quite different heat transfer processes, and the multi-dimensional effects are pronounced in the pulse tube. As shown in Fig. 12(a), for Case 2 in which the MCSPTC operates at 90 Hz, the isotherms inside the pulse tube bend dramatically, which indicates that the gas displacer in the middle segment cannot isolate the gases at two ends from each other anymore, thereby resulting in a strong mixing between warm and cold fluids which would considerably deteriorate the cooling performance. In striking contrast to Case 2, for Case 6 in which the MCSPTC operates at 140 Hz, as shown in Fig. 12(c), the isotherms are almost vertical with only slight distortions, which indicates that the least mix is introduced among these cases and the gas displacer can effectively isolate the gases at two ends, and thus a much better performance can be expected.

In Case 4 at 110 Hz shown in Fig. 12(b) and Case 7 at 150 Hz in Fig. 12(d), either of the isotherms inside the pulse tube bend more severely than those in Case 6 at 140 Hz, which indicates that the moderate temperature distortions caused by either lower or higher operating frequency would lead to a worse performance than that at the optimal operating frequency. However, it is evident that in both cases, the gas displacers still work normally and the gases at cold and warm ends do not mix dramatically as happened in Case 2. The phenomena may explain that moderately good cooling performances are achieved in both Case 4 and Case 7.

However, when the frequency increases up to 160 Hz, as shown in Fig. 12(e), an obviously different phenomenon happens. In the middle segment of the pulse tube, large temperature gradients in radial directions occur, in which the fluids near the axis are much warmer than those near the tube wall. It indicates that the gas displacer has nearly been punctured from the warm end, which would undermine the cooling performance. In addition, it is observed that the cold fluids account for the less ratio of the whole volume with the increasing frequency. The reasons will be explained when the velocity streamlines are discussed later. Much more obvious phenomena can be observed in Case 9 with a higher frequency of 170 Hz, as shown in Fig. 12(f).

In order to provide a clearer display about the effects of the operating frequency on the flow patterns in the pulse tube, the velocity streamlines are simulated in a detailed way. Fig. 13(a) and (b) show the transient velocity streamlines at two different moments during the expansion to compression process and the reversed process respectively at 90 Hz in Case 2. A considerably large fully developed vortex occurs in the middle segment of the pulse tube for both moments, accounting for about 80% of the whole volume, which would lead to a strong mixing between warm and cold fluids, thereby greatly deteriorating the cooling performance.

Fig. 14(a) and (b) show the transient velocity streamlines at 140 Hz in Case 6, in the expansion to compression process and the reversed process, respectively. Two medium-sized vortices appear near two ends in the cases, respectively. The vortex near the cold end is generated before the end of the expansion process and then developed from the axis to the wall in the radial direction, and finally vanished after the compression process begins, as shown in Fig. 14(a). The other vortex near the warm end experiences a totally inverse process, as shown in

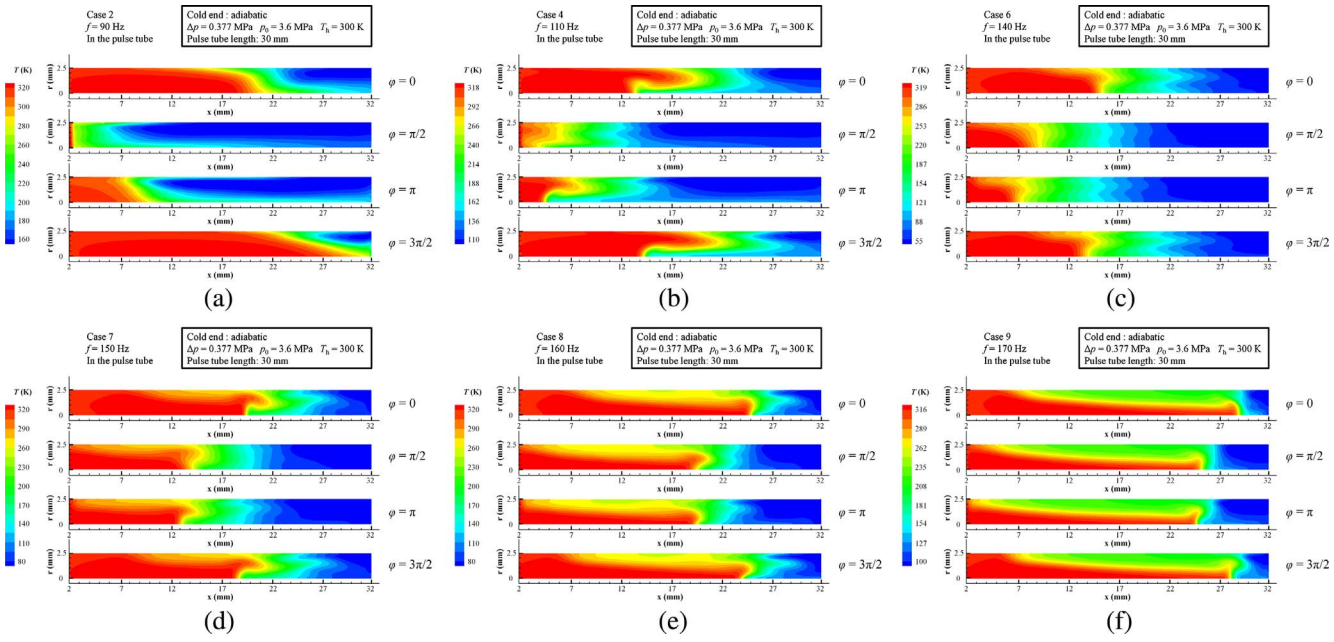


**Fig. 12.** Temperature contours inside the pulse tube during one cycle in Cases 2, 4 and 6–9. (a) 90 Hz. (b) 110 Hz. (c) 140 Hz. (d) 150 Hz. (e) 160 Hz. (f) 170 Hz.

Fig. 14(b). The size of each vortex is about half of the whole volume, and the left one is slightly larger than its right counterpart because the axial velocity amplitude near the warm end is larger than that near the cold end shown in Fig. 8. Therefore, the gas displacer in the middle segment can effectively isolate two ends from each other, thereby resulting in the satisfactory performance.

Fig. 15(a) and (b) show the transient velocity streamlines at 170 Hz in Case 9. It should be noted that, the two vortices are much smaller in size than those in Case 6, especially for the right one, which is mainly caused by the smaller velocity amplitudes near both two ends at 170 Hz than those at 140 Hz, as shown in Fig. 8. It can explain the phenomenon that the cold fluids account for the less volume of the pulse tube with the increasing frequency as discussed above. In addition, as shown in Fig. 15(a), the streamlines near the warm end are downward sloping during the expansion to compression process, which indicates that the warmer fluids flow from the warm end to the axis, sometimes nearly punctures the gas displacer from the warm end, thereby creating larger temperature gradients in radial directions in the middle segment of the pulse tube, as shown in Fig. 12(f). Moreover, as shown in Fig. 15(b), several small vortices appear near the cold end when the expansion process begins, which are probably caused by the inverse flow due to the coaxial geometry, and thus the similar phenomenon is not observed near the cold end.

### 2.3. Effect of pulse tube length at 170 Hz

As discussed above, when the operating frequency increases up to 170 Hz, the flow in the middle segment of the pulse tube becomes considerably weak, and the sizes of two vortices at both ends account for too smaller proportions of the whole pulse tube. Therefore, in order to enhance the oscillating flow and heat transfer at such a high frequency, several shorter pulse tubes are employed in Cases 10–13 while keeping the operating frequency at 170 Hz. Table 4 gives the input PV powers in Cases 9–13. Similar to the discussions for Table 3, the input PV power only changes slightly, and thus the comparisons for the cases are reasonable.

Fig. 16 provides the time-averaged no-load temperatures as a function of the pulse tube length at a constant frequency of 170 Hz. The no-load temperature decreases with the pulse tube length decreasing from 30 mm to 20 mm. The best performance occurs in Case 13 with the 20 mm pulse tube, which achieves a no-load temperature of 69.5 K, about 28.5 K lower than that in Case 9. The changing tendency indicates that the cooling performance can be improved dramatically by shortening the pulse tube when the operating frequency is much higher than the optimum.

Fig. 17 shows the temperature contours inside the pulse tube in four different situations during one cycle in Case 13 with the 20 mm pulse tube. It is observed that, in the middle segment of the pulse tube, the temperature gradients in radial directions are much smaller than those

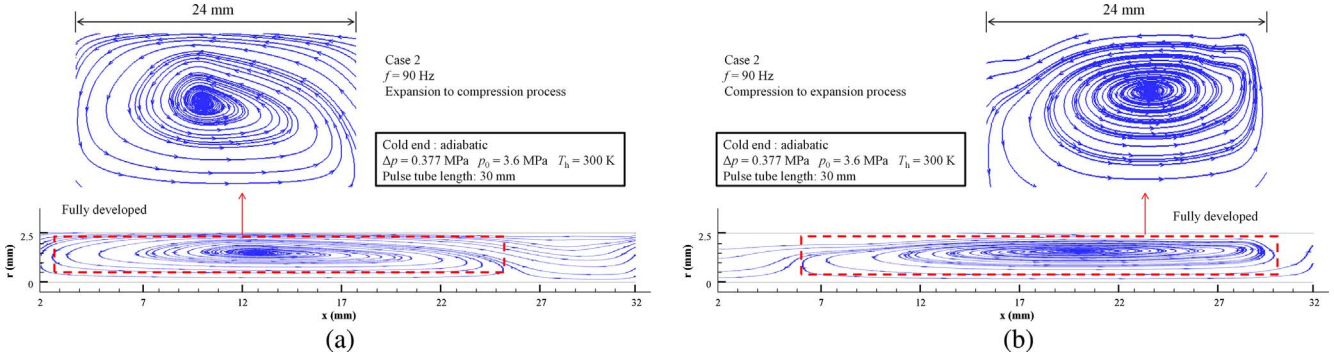


**Fig. 13.** Transient velocity streamlines in Case 2. (a) During the expansion to compression process. (b) During the compression to expansion process.

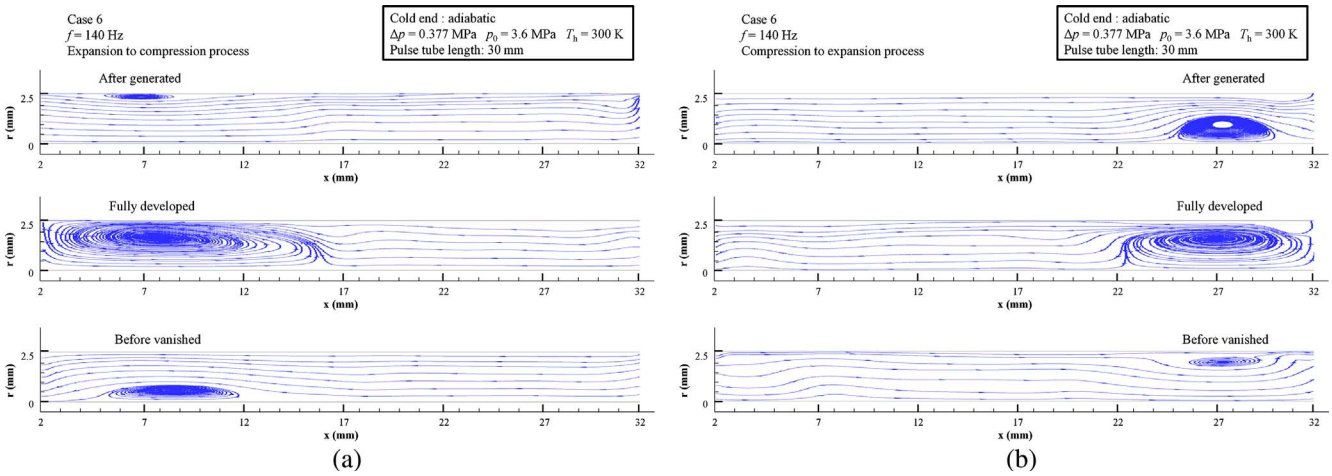


**Fig. 14.** Transient velocity streamlines in Case 6. (a) During the expansion to compression process. (b) During the compression to expansion process.

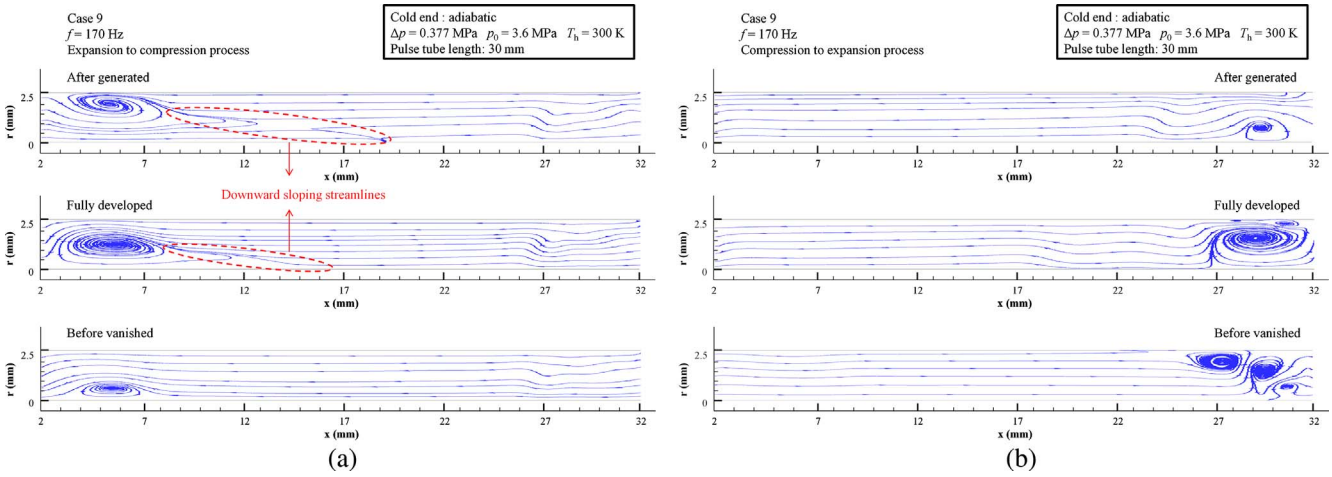


**Fig. 15.** Transient velocity streamlines in Case 9. (a) During the expansion to compression process. (b) During the compression to expansion process.

**Table 4**
Input PV power in cases 9–13.

| Case number | Pulse tube length (mm) | $\lvert\dot{m}_{ai}\rvert$ (g/s) | $\langle\dot{W}_{pv}\rangle$ (W) |
|---|---|---|---|
| 9 | 30 | 1.35 | 43.5 |
| 10 | 27.5 | 1.37 | 43.7 |
| 11 | 25 | 1.38 | 43.8 |
| 12 | 22.5 | 1.40 | 44.0 |
| 13 | 20 | 1.41 | 44.2 |

in Case 9 shown in Fig. 12(f), and the gas displacer is not punctured from the warm end, which avoids the strong mix between warm and cold fluids, thereby substantially enhancing the cooling performance. In addition, the cold fluids account for about 40% of the whole volume, which is nearly twice as much as that in Case 9 with the 30 mm pulse tube. It should be noted that, the temperature contours during one cycle in this case are very similar to those in Case 7 shown in Fig. 12(d), and the difference of the no-load temperature between the two cases is only about 10 K, which indicates that the heat transfer processes in Case 13 at 170 Hz with the 20 mm pulse tube are roughly similar to those in Case 7 at 150 Hz with the 30 mm pulse tube.

Fig. 18(a) and (b) show the transient velocity streamlines in Case 13. Compared with Fig. 15(a) and (b), the sizes of two vortices at both ends account for larger proportions of the whole pulse tube, which is in line with the phenomenon that the cold fluids account for the more volume, as shown in Fig. 17. The downward sloping streams can also be

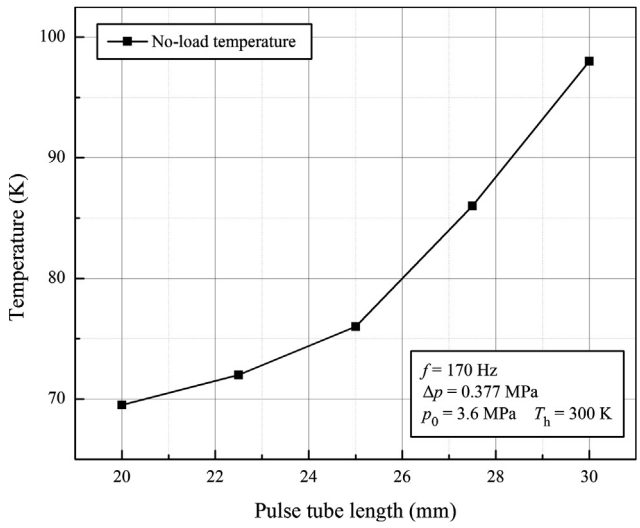


**Fig. 16.** Time-averaged no-load temperature at 170 Hz as a function of the pulse tube length.

observed in Fig. 18(a), however, the proportions in radial directions are much larger than those in Fig. 15(a), resulting in the much smaller radial temperature gradients in the middle segment of the pulse tube as shown in Fig. 17, thereby avoiding the puncture in the gas displacer from the warm end, which significantly improves the flow and heat

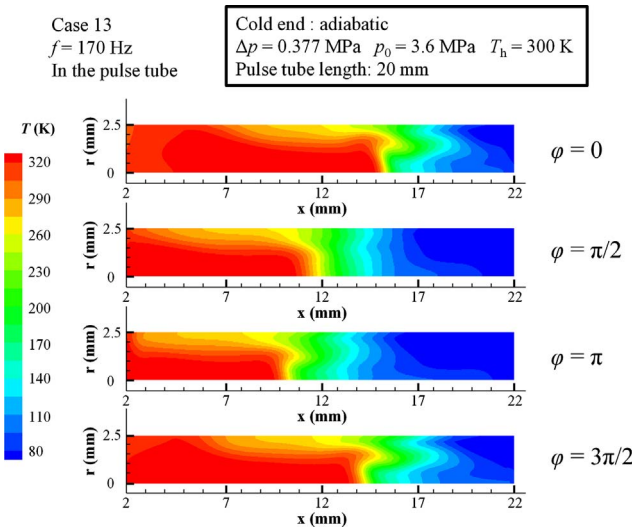


**Fig. 17.** Temperature contours inside the pulse tube during one cycle in Case 13.

transfer processes and thus enhances the cooling performance.

## 3. Experimental verifications

In order to verify the validity of the above simulation results, a MCSPTC operating at 90–170 Hz without either double-inlet or multi-bypass has been manufactured and tested. As shown in Fig. 19, based on a 300 W mid-size compressor designed in the same group, a micro moving-coil linear compressor is developed by the modified scaling principles in which the scaling factors of several key components are modified to adapt to the micro design. Its resonant frequency increases from 55 Hz to 140 Hz, and the mass decreases from 8.0 kg to 0.8 kg.

Fig. 20 shows a photograph of the developed MCSPTC. The geometrical dimensions of the micro coaxial cold finger and the inertance tubes are the same as the simulated values in the above CFD model, in which the length of the pulse tube is fixed at 30 mm. The total mass of the cooler is about 1.1 kg, which is a little more than the estimated weight of 920 g. The AC power supply is used to power the micro linear compressor and measure the input electric parameters simultaneously.


**Fig. 19.** A photograph of the developed micro linear compressor and the mid-size linear compressor.

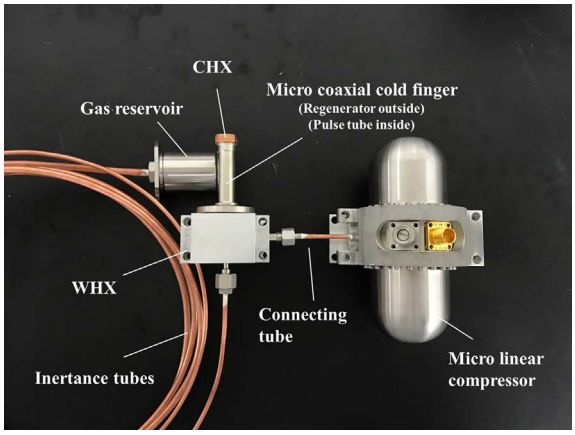


**Fig. 20.** A photograph of the developed MCSPTC.

The temperature acquisition is employed to monitor the coldtip temperature, and the cooling capacity is controlled by the heat load acquisition. The heat generated from the micro linear compressor and the warm heat exchanger is removed by forced air and circulating water

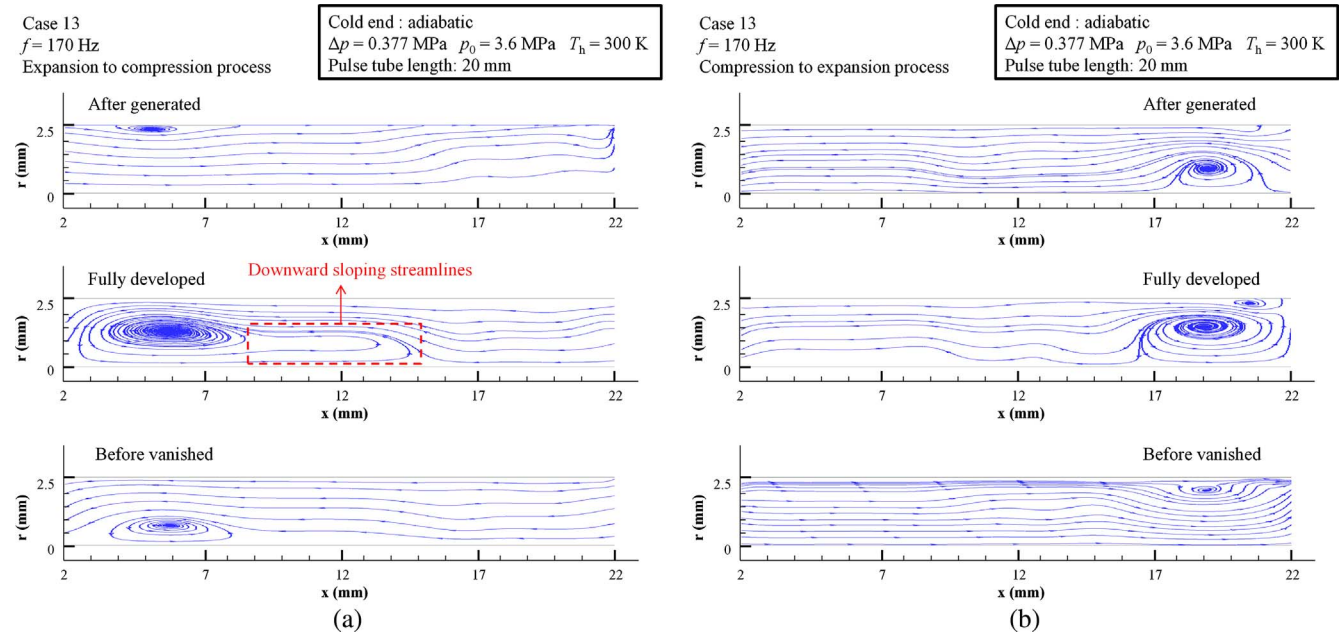


**Fig. 18.** Transient velocity streamlines in Case 13. (a) During the expansion to compression process. (b) During the compression to expansion process.

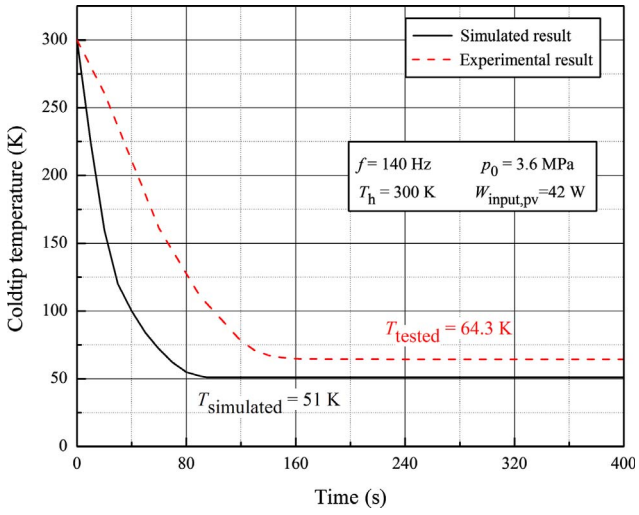


**Fig. 21.** Simulated and tested cool down curves at 140 Hz.

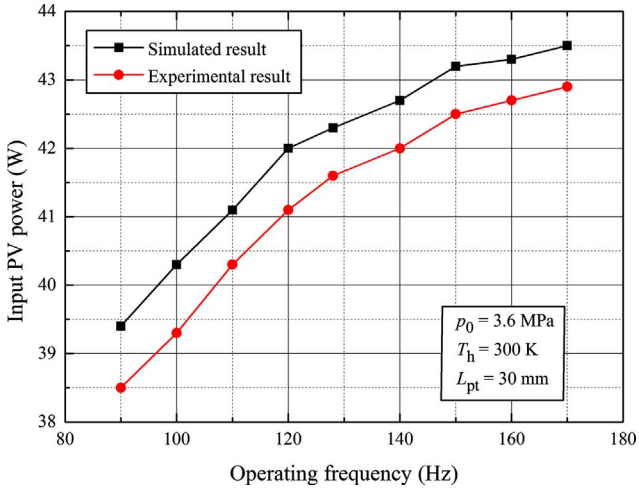


**Fig. 22.** Simulated and tested input PV power as a function of the operating frequency.

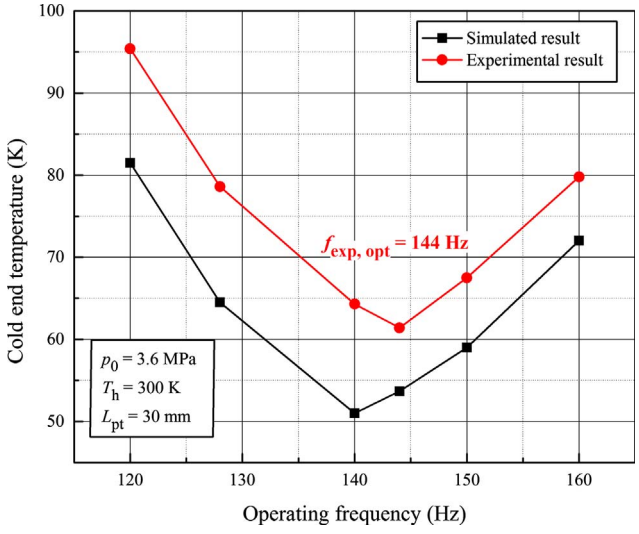


**Fig. 23.** Simulated and tested no-load temperatures as a function of the operating frequency.

cooling, respectively. The vacuum pump is employed to provide the vacuum environmental for the micro coaxial cold finger.

The corresponding experiments are carried out to verify the simulated results. The initial operating frequency and the charging pressure are set to 140 Hz and 3.6 MPa, respectively. The motor efficiency $\eta$ can be estimated by:

$$\eta = (\dot{W}_e - I^2R)/\dot{W}_e \tag{3}$$

where $\dot{W}_e$ is the input electric power, $I$ is the input current, $R$ is the coil resistance in the compressor. Therefore, the practical input PV power can be calculated by

$$\dot{W}_{pv} = \eta\dot{W}_e \tag{4}$$

The initial input electric power is about 59 W with the motor efficiency of 71.3%, and therefore the PV power transferred to the inlet of the aftercooler is up to about 42.0 W, which is nearly the same as that in the above CFD model shown in Table 3. As a result, the input conditions and the operating parameters between the simulation and the experiment are considered to be identical.

Fig. 21 shows the comparisons between the simulated and experimental cooldown curves at the operating frequency of 140 Hz. It can be observed that, when the input PV power is 42.0 W, the tested no-load temperature can reach to 64.3 K, with 13.3 K higher than that in the corresponding simulation of Case 6. Furthermore, it takes about 280 s from the initial temperature of 300 K down to the steady value in the experiment, which is much longer than the simulated cooldown time of 95 s. The discrepancies on both the no-load temperature and the cooldown time between simulation and experiment can be explained by the following two reasons. One reason is that the regenerator and heat exchangers in the simulation employ the thermal equilibrium model, and therefore the imperfect transfer losses between the working fluid and the solid matrix in these components are ignored. The other reason is that the heat transfer between the heat exchangers and the environment in the model is assumed to be ideal, which substantially accelerates the simulated cooling rate.

In order to keep the same input conditions for both simulations and experiments, the input voltage and electric power are adjusted with the variation of the operating frequency. Fig. 22 shows the comparisons between simulated and tested input PV powers at different operating frequencies. It can be observed that, the tested input PV power at each frequency is about 0.8 W lower than the simulated one, which ensures that the comparisons between simulated and experimental cooling performances are reasonable.

Fig. 23 shows both simulated and tested no-load temperatures as a function of the operating frequency. It can be seen that the changing tendency in the experiment is in good agreement with that in the simulation. The tested optimal frequency is 144 Hz, with only 4 Hz higher

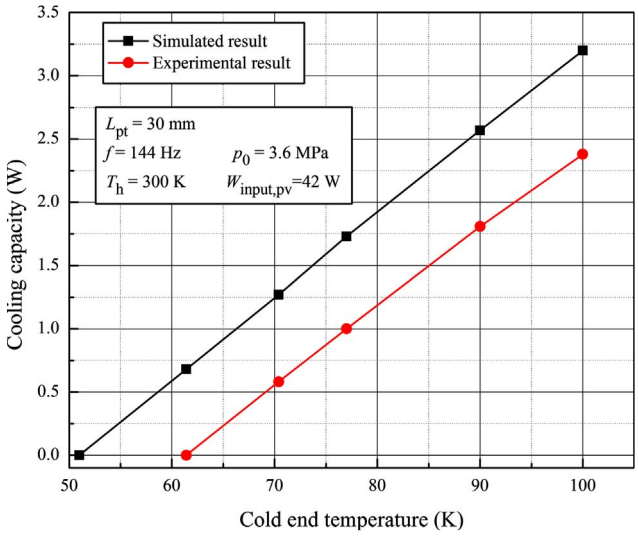


**Fig. 24.** Simulated and tested cooling capacities below 100 K at 144 Hz.

than the simulated result. The tested no-load temperature is down to 61.4 K at the optimal frequency. Either higher or lower operating frequency will undermine the cooling performance, which can prove that the above discussions in both temperature contours and velocity streamlines are reasonable.

The typical cooling capacities below 100 K are compared between simulation and experiment at the operating frequency of 144 Hz. The reject temperature and the input PV power are maintained at 300 K and 42 W, respectively. As shown in Fig. 24, the changing tendencies of the tested results also agree well with those of the simulated ones. In the experiment, the developed MCSPTC can achieve the cooling capacities of 0.58 W, 1.0 W and 1.8 W with the coldtip temperature of 70 K, 77 K and 90 K, respectively, all of which are about 0.7 W lower than the corresponding simulated results. The discrepancies are mainly caused by the following three reasons. Firstly, the operating frequency of 144 Hz is slightly different from the resonant frequency of 140 Hz for the micro linear compressor, thereby decreasing the motor efficiency to some extent. Secondly, the mismatch of the axial temperature profiles between the regenerator and the pulse tube is ignored in the CFD model, which can generate additional conductive heat losses in radial direction in the practical MCSPTC. Thirdly, the thermal equilibrium model employed in both the regenerator and the heat exchangers is also responsible for the discrepancies between the simulated and tested results.

## 4. Conclusions

Based on the two-dimensional axisymmetric CFD model and the developed micro coaxial Stirling-type pulse tube cryocooler (MCSPTC), this paper presents the systematic simulations and the experimental verifications of the oscillating flow and heat transfer processes in the MCSPTC operating at 90–170 Hz. It uses neither double-inlet nor multi-bypass while the inertance tube with a gas reservoir becomes the only phase-shifter.

The flow characteristics and temperature variations at the inlet, midpoint and outlet cross-sections of the pulse tube are simulated first based on the basic case operating at 128 Hz with a 30 mm-long pulse tube. The results show that the axial velocity increases from cold to warm end, and the impedance near the warm end is a little higher than that near the cold end. The temperature oscillations at both ends are far away from the sinusoidal wave, which are mainly caused by the complicated heat transfer between the pulse tube and the corresponding heat exchangers.

The effects of the operating frequency ranging from 90 to 170 Hz on the oscillating flow and heat transfer processes inside the pulse tube are investigated. The results indicate that there exists an optimum frequency for given dimensions. A frequency much lower than the optimal value would lead to a strong mixing between warm and cold fluids, which would considerably deteriorate the cooling performance. However, a frequency much higher than the optimal value would produce the downward sloping streams which flow from the warm end to the axis, which nearly puncture the gas displacer from the warm end, thereby creating larger temperature gradients in radial directions in the middle segment of the pulse tube and thus undermining the cooling performance.

The influence of the pulse tube length on the temperature and velocity when the frequencies are much higher than the optimal one are also discussed. In that case, a pulse tube much shorter than the original value would substantially decrease the radial temperature gradients in the middle segment, thereby avoiding the puncture in the gas displacer from the warm end, which significantly improves the flow and heat transfer processes and thus enhances the cooling performance.

A 1.1 kg MCSPTC operating at 90–170 Hz is worked out and the corresponding experiments are carried out. With the input electric power of 59 W, the developed MCSPTC operating at the tested optimal frequency of 144 Hz can achieve a no-load temperature of 61.4 K and a cooling capacity of 1.0 W at 77 K. The general changing tendencies of experimental results are in good agreement with the simulations. The acceptable discrepancies between simulated and tested results are also analyzed, which mainly result from the thermal equilibrium model employed in both the regenerator and the heat exchangers, the additional conductive heat losses in radial direction between the regenerator and the pulse tube in the practical MCSPTC, and the slight difference between the actual and the resonant frequency of the micro linear compressor.

The above theoretical and experimental studies will help to thoroughly understand the underlying mechanism of the inertance MCSPTC operating at very high frequencies.

## Acknowledgements

The work is financially supported by The National Basic Research Program of China (No. 2013CB632802), The Aeronautical Science Foundation of China (No. 20162490005) and The Science and Technology Commission of Shanghai Municipality (No. 15521104900). The work was finished during the first author pursued his doctoral degree in State Key Laboratory of Infrared Physics, Shanghai Institute of Technical Physics, Chinese Academy of Sciences under the supervision of Professor Haizheng Dang.

## References

[1] Radebaugh R, Garaway I, Veprik AM. Development of miniature, high frequency pulse tube cryocoolers. In: Infrared technology and applications XXXVI, 5–9 April 2010, SPIE – The International Society for Optical Engineering, USA, 2010, p. 76602J (76614 p).
[2] Ross Jr. RG. Space coolers: a 50-year quest for long life cryogenic cooling in space. In: Timmerhaus KD, Reed RP, editors. Cryogenic engineering: fifty years of progress. New York: Springer Publishers; 2006. p. 225–84.
[3] Raab J, Tward E. Northrop Grumman space systems cryocooler overview. Cryogenics 2010;50:572–81.
[4] Dang HZ. Development of high performance moving-coil linear compressors for space Stirling-type pulse tube cryocoolers. Cryogenics 2015;68:1–18.
[5] Dang HZ. 40 K single-stage coaxial pulse tube cryocoolers. Cryogenics 2012;52:216–20.
[6] Yuan SWK, Curran DGT, Cha JS. A non-tube inertance device for pulse tube cryocoolers. Adv Cryog Eng 2010;55:143–8.
[7] Peterson RB, Al Hazmy M. Size limits for Stirling cycle refrigerators and cryocoolers. Adv Cryog Eng 1998;43:997–1002.
[8] Shire JM, Mujezinovic A, Phelan PE. Investigation of microscale cryocoolers. Cryocoolers 1999;10:663–70.
[9] Radebaugh R, O'Gallagher A. Regenerator operation at very high frequencies for micro-cryocoolers. Adv Cryog Eng 2006;51:1919–28.
[10] Petach M, Waterman M, Tward E, et al. Pulse tube microcooler for space applications. Cryocoolers 2007;14:89–93.
[11] Petach M, Waterman M, Pruitt G, et al. High frequency coaxial pulse tube microcooler. Cryocoolers 2009;15:97–103.
[12] Nguyen T, Petach M, Michaelian M, et al. Space micro pulse tube cooler. Cryocoolers 2011;16:97–101.
[13] Durand D, Tward E, Toma G, et al. Efficient high capacity space microcooler. Cryocoolers 2014;18:59–64.
[14] Olson JR, Champagne P, Roth E, et al. Microcryocooler for tactical and space applications. Adv Cryog Eng 2014;59:357–64.
[15] Nast TC, Roth E, Olson JR, et al. Qualification of lockheed Martin micro pulse tube cryocooler to TRL6. Cryocoolers 2014;18:45–50.
[16] Frank D, Champagne P, Will E, et al. Extended range of the lockheed Martin coaxial micro cryocooler. Cryogenics 2016;74:55–8.
[17] Vanapalli S, Lewis M, Grossman G, et al. Modeling and experiments on fast cooldown of a 120 Hz pulse tube cryocooler. Adv Cryog Eng 2008;53:1429–36.
[18] Lopes D, Duval JM, Charles I, et al. Design and characterization of very high frequency pulse tube prototypes. Adv Cryog Eng 2012;57:1487–94.
[19] Ashwin TR, Narasimham GSVL, Jacob S. CFD analysis of high frequency miniature pulse tube refrigerators for space applications with thermal non-equilibrium model. Appl Therm Eng 2010;30:152–66.
[20] Antao DS, Farouk B. Numerical and experimental characterization of the inertance effect on pulse tube refrigerator performance. Int J Heat Mass Transf 2014;76:33–44.
[21] Dang HZ, Zhao YB. CFD modeling and experimental verification of a single-stage coaxial Stirling-type pulse tube cryocooler without either double-inlet or multi-bypass operating at 30–35 K using mixed stainless steel mesh regenerator matrices. Cryogenics 2016;78:40–50.
[22] Zhao YB, Dang HZ. CFD simulation of a miniature coaxial Stirling-type pulse tube cryocooler operating at 128 Hz. Cryogenics 2016;73:53–9.
[23] Gedeon D. DC gas flows in Stirling pulse tube cryocoolers. Cryocoolers 1997;9:385–92.
[24] Olson JR, Swift GW. Acoustic streaming in pulse tube refrigerators: tapered pulse tubes. Cryogenics 1997;37:769–76.